Measurement Science
and Technology

PAPER • **OPEN ACCESS**

Wireless and passive pressure detection using magneto-mechanical resonances in process engineering

To cite this article: Timo Merbach *et al* 2025 *Meas. Sci. Technol.* **36** 085109

OPEN ACCESS
IOP Publishing
Measurement Science and Technology
Meas. Sci. Technol. **36** (2025) 085109 (11pp)
https://doi.org/10.1088/1361-6501/adf2c8

Wireless and passive pressure detection using magneto-mechanical resonances in process engineering

Timo Merbach[1,*], Felix Kexel[1], Jonas Faltinath[2,3], Martin Möddel[2,3], Michael Schlüter[1], Tobias Knopp[2,3,4] and Fabian Mohn[2,3]

[1] Institute of Multiphase Flows, Hamburg University of Technology, Hamburg, Germany
[2] Institute for Biomedical Imaging, Hamburg University of Technology, Hamburg, Germany
[3] Section for Biomedical Imaging, University Medical Center Hamburg-Eppendorf, Hamburg, Germany
[4] Fraunhofer Research Institution for Individualized and Cell-based Medical Engineering IMTE, Lübeck, Germany

E-mail: timo.merbach@tuhh.de

Received 14 February 2025, revised 30 June 2025
Accepted for publication 22 July 2025
Published 7 August 2025

Abstract

A custom-developed magneto-mechanical resonator (MMR) for wireless pressure measurement is investigated for potential applications in process engineering. The MMR sensor utilises changes in the resonance frequency caused by pressure on a flexible 3D printed membrane. The thickness of the printed membrane plays a crucial role in determining the performance and sensitivity of MMRs and can be tailored to meet the requirements of specific applications. The study includes static and dynamic measurements to determine the pressure sensitivity and temporal resolution of the sensor. The results show a minimum sensitivity of 0.06 Hz mbar^{-1} and are in agreement with theoretical calculations and measurements. The maximum sensor readout frequency is 2 Hz in this study. Additionally, the temperature dependence of the sensor is investigated, revealing a significant dependence of the resonance frequency on temperature. The developed MMR offers a promising and versatile method for precise pressure measurements in process engineering environments.

Keywords: pressure sensor, magneto-mechanical resonator, sensing, resonance frequency, magnet-to-magnet distance

* Author to whom any correspondence should be addressed.

Nomenclature

Arabic symbols

D_C	column diameter (m)
D_H	hose diameter (m)
D_{MMR}	MMR diameter (m)
$D_{MMR,\,R}$	rotator diameter (m)
$D_{MMR,\,S}$	stator diameter (m)
D_R	reservoir diameter (m)
d_0	initial distance (m)
d_e	edge-to-edge distance (m)
d_m	mass-centred distance (m)
Δd	stretch distance (m)
F	force (N)
f_{nat}	natural frequency (Hz)
g	gravitational acceleration (m s^{-2})
h	height for hydrostatic pressure (m)
h_1	height at position ① (m)
h_2	liquid level at position ② (m)
h_C	column height (m)
h_E	height of hose extension (m)
h_{MMR}	MMR height (m)
$h_{MMR,\,S}$	stator height (m)
h_R	reservoir height (m)
$h_{R,\,Ref}$	reference height for reservoir (m)
$h_{MMR,\,Ref}$	reference height for MMR (m)
h_S	height for outlet dynamics (m)
I	inertia (kg m^2)
L	inductance (H)
M_R	rotator magnetic moments (A m^2)
M_S	stator magnetic moments (A m^2)
m	mass (kg)
n	number of measurements (−)
p	pressure (Pa)
p_0	atmospheric pressure (Pa)
p_1	pressure at position ① (Pa)
p_2	pressure at position ② (Pa)
R_S	specific gas constant (J $kg^{-1}K^{-1}$)
R	resistance (Ω)
r^2	coefficient of determination (−)
s	membrane thickness (m)
T	temperature (°C)
T_0	ambient temperature (°C)
t	time (s)
t_{rx}	receive time (s)
t_{tx}	transmit time (s)
V	volume (m^3)
$\dot{V}$	volumetric flow rate ($m^3\,s^{-1}$)
v_1	liquid velocity at position ① (m s^{-1})
v_2	liquid velocity at position ② (m s^{-1})

Greek symbols

ζ	resistance coefficient (−)
μ_0	vacuum permeability (H m^{-1})
ρ	fluid density (kg m^{-3})

1. Introduction

In process engineering, hydrodynamic process data, such as residence times, mixing times, and volume flow exchange rates, are crucial for scale-up, process control, and optimisation [1–3]. In both industrial and academic settings, conventional sensors are typically mounted on the exterior of the vessel and rely on a Eulerian approach for tracking. In contrast, Lagrangian sensors are deployed directly within the moving fluid inside the vessel, providing insights into the internal process conditions. Numerous research groups are actively developing such sensors, namely Lagrangian sensor particles, particularly for the application in bioreactors [4–8]. For such active sensors, ensuring the power supply remains a challenge [9]. The most significant limitation lies in determining the sensor's position within the vessel. At present, only axial position data, acquired through optical access or inferred from hydrostatic pressure, can be utilised for localisation purposes [4–7]. The obtained data is limited to two-dimensional information. This is insufficient for a comprehensive investigation of biochemical or pharmaceutical processes, as numerical and experimental studies have demonstrated the presence of spatial heterogeneities in bioreactors [10, 11]. These heterogeneities influence the bioprocess performance by subjecting microorganisms to fluctuating environmental conditions [12–14]. To enable effective process optimisation, it is essential to develop a measurement sensor that allows for the acquisition of three-dimensional spatial information combined with key process parameters such as pressure and temperature under product-relevant and industrial conditions [15].

The medical field is also confronted with the challenge of monitoring the position and orientation of medical instruments within the human body, necessitating the acquisition of radial and axial information. In response to this need, a novel wireless and passive sensor based on magneto-mechanical resonance was recently introduced [16]. While this sensor is focused on miniaturisation for medical applications such as endoscopy, surgery, implantation, and vascular interventions to measure position and orientation (6 degrees of freedom), it also has huge potential for technical applications such as process engineering for which it has not yet been utilised so far. In short, the so-called magneto-mechanical resonator (MMR) can be used for tracking by measuring its directional response to a weak magnetic field excitation. In addition, the MMR allows for sensing, since the internal magnet distance affects its resonance frequency [17, 18]. Coupling this distance to an additional mechanical sensing mechanism allows for determining an environmental parameter such as temperature, pressure, magnetic fields or viscosity.

One crucial aspect of data analysis is the possibility of co-registering wireless sensor data with spatial tracking information. As demonstrated in [16], spatial tracking with MMRs has been successfully achieved. However, the integration of tracking and sensing processes introduces additional challenges in signal processing that are beyond the scope of the present

study. Instead, the study is focused solely on investigating the sensing capabilities of the MMR sensor in the context of process engineering as a proof of concept. Such applications present a number of additional challenges, including electromagnetic interference, distorted supply currents, non-transparent stainless-steel vessels, and extreme temperature as well as pressure conditions. Consequently, this study develops and tests an MMR sensor for measuring pressure in a liquid column under a range of such conditions. It focuses on the sensor's sensitivity, measurement range, real-time accuracy, and temperature cross-sensitivity. Three experimental approaches are used: static experiments with constant pressure, dynamic experiments measuring pressure variation, and temperature-changing MMR tests.

2. Material and methods

A refillable acrylic column is employed to establish different pressure levels on the MMR, while the passive natural resonance of the MMR is excited inductively and received using a set of coils, located on the outside of the column. The following sections will provide a detailed explanation of each component of the setup.

2.1. Hydrodynamic setup

Figure 1 shows the schematic flow diagram of the test bench. A transparent cylindrical column with an inner diameter of $D_C = 70\,\text{mm}$ is employed for the experiments. The column has a height of $h_C = 1.5\,\text{m}$, extended by a hose with a length of $h_E = 5\,\text{m}$. This setup follows Pascal's paradox, where the pressure depends solely on the height of the column, regardless of the volume or shape of the tank [19, 20]. A measuring tape is affixed externally along the entire length to facilitate optical height measurement (with an uncertainty of $\pm 1\,\text{cm}$), thereby enabling subsequent hydrostatic pressure determination. Additionally, due to the optical access provided by the column and the MMR, a camera using backlight imaging is employed to analyse the edge-to-edge distance d_e between the magnets during the experiment, which further validates the measurement principle. The MMR is mounted on the base of a column at a height of $h_{\text{MMR, Ref}} = 0.53\,\text{m}$ above the outlet. Figure 2(a) shows the configuration surrounding the MMR, depicting its arrangement on the test bench.

The column is filled with deionised water kept at a constant temperature of $T = (21.1 \pm 0.5)\,^\circ\text{C}$, with a corresponding fluid density of $\rho = (998.0 \pm 0.1)\,\text{kg m}^{-3}$ [21]. A reservoir ($D_R = 0.29\,\text{m}, h_R = 2.0\,\text{m}$) is connected to the column to supply the latter with deionised water, the two components connected by the principle of communicating liquid levels. The deionised water is conditioned to ambient temperature for several hours in the reservoir, ensuring thermal equilibrium between the deionised water and the surrounding air. This preparation eliminates thermal effects in the column and MMR, preventing temperature-induced variations in the results.

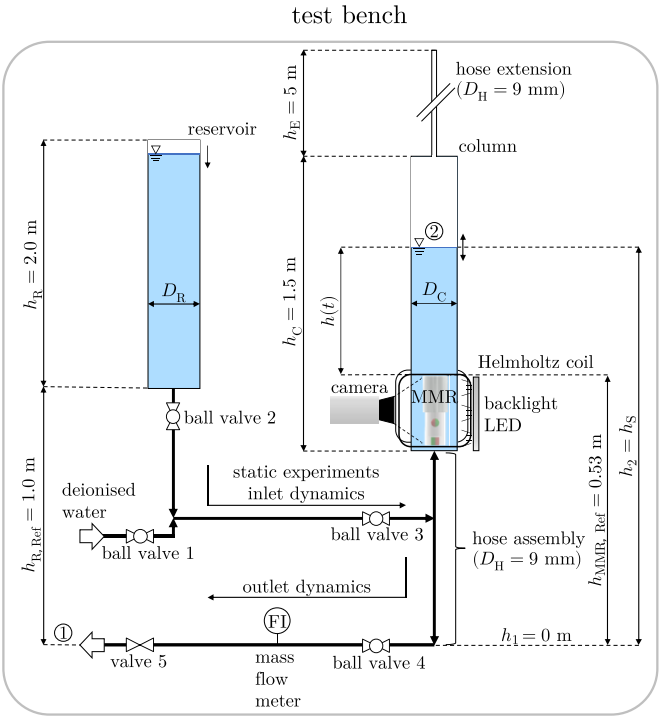

Figure 1. Test bench for hydrostatic and hydrodynamic experiments. Schematic flow diagram of the test bench detailing the column, reservoir, and associated peripheral systems.

In static experiments, deionised water is introduced from the reservoir via ball valves 2 and 3, illustrated in figure 1. The liquid height above the MMR h is kept constant by closing ball valve 3. At constant liquid height, the MMR is excited and the natural frequency is received, while the corresponding height is simultaneously determined via optical height measurement. In this way, different hydrostatic pressures are set and measured. In static experiments where the needed hydrostatic pressure exceeds the reservoir's height, unconditioned deionised water is used.

However, the added volume of unconditioned water is minimal, as the column is already filled and the inner diameters of the hoses located above it are significantly smaller ($D_C \gg D_H = 9\,\text{mm}$). Additionally, a waiting period allows temperature differences to equilibrate.

Moreover, dynamic experiments are conducted, in which the inlet and outlet dynamics are characterised. In case of the inlet dynamics, the column is filled in the same manner as in the static experiments. Filling the deionised water from the bottom of the column ensures an immediate pressure increase at the sensor for accurate and responsive tracking of liquid level changes. This way promotes a smooth, continuous rise in liquid without significant surface turbulence. For the outlet dynamics, the outlet of the column is connected to a hose assembly located below the column. The hoses also have an inner diameter of $D_H = 9\,\text{mm}$. The segment of the assembly corresponding to the outlet dynamics features a ball valve (ball valve 4), followed by a Coriolis mass flow meter (Promass 80,

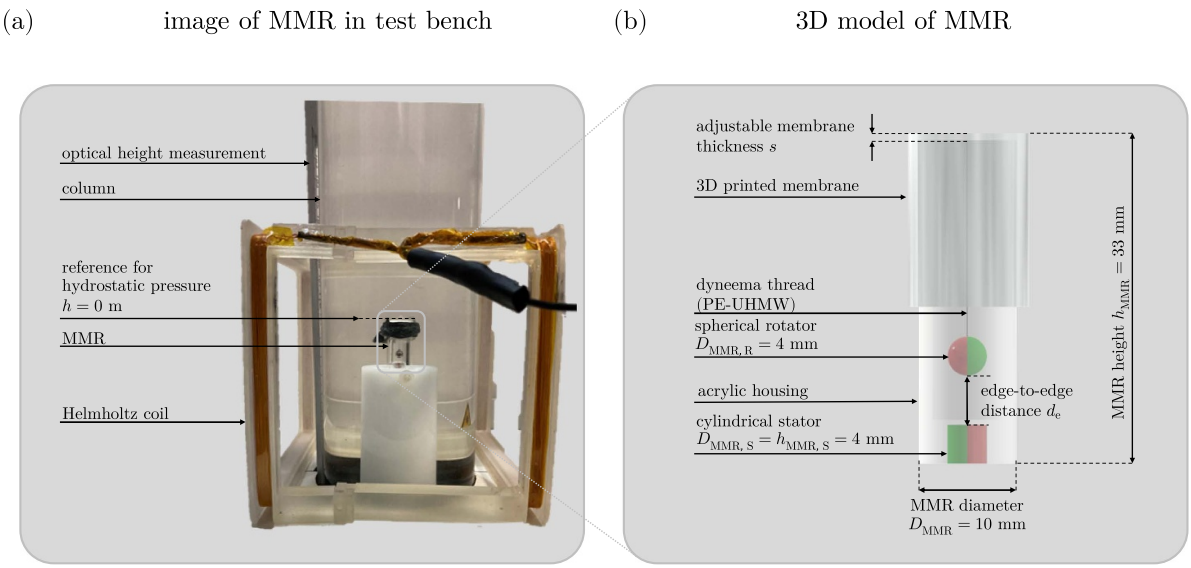

Figure 2. MMR setup and implementation on the test bench. In (a), MMR on the test bench integrated with the square-shaped Helmholtz coil and fixed within the column for the purpose of measuring the hydrostatic pressure. 3D model of the MMR showcasing the 3D printed membrane, rotator, and stator in (b).

Endress + Hauser, Switzerland) to measure the outlet flow, and an additional valve (valve 5), which is maintained in a fixed position. To discharge the column, ball valve 4 is fully opened, resulting in a consistent and reproducible outlet time.

Inlet and outlet dynamics are based on established hydrodynamic principles, as optical height measurement of rapidly changing liquid levels is challenging. Only the upper and lower levels are determined optically, while the dynamics are assessed by recording the time taken to fill or discharge a 1 m liquid column.

2.2. Hydrostatic and hydrodynamic fundamentals

The hydrostatic pressure $p(h)$ on the MMR is directly proportional to the height of the liquid level above the MMR h as described in equation (1). The reference height for the hydrostatic pressure is defined at the top of the MMR membrane, as shown in figure 2(a). The hydrostatic pressure is given by Pascal's law as

$$p(h) - p_0 = \rho g h, \tag{1}$$

where $p_0 = 1\,\mathrm{atm}$ denotes the atmospheric pressure and $g = 9.81\,\mathrm{m\,s^{-2}}$ the gravitational acceleration [19]. As a fluid-specific parameter, the density ρ appears in equation (1), which makes the equation applicable not only to water, as used in this study, but also to various other fluids such as industrially relevant media or viscous fluids. All pressures are given as relative pressures in this paper.

In addition, the inlet and outlet dynamics are characterised mathematically, as detailed below. For the inlet dynamics, the volumetric flow rate $\dot{V}$ is assumed to be constant. This assumption is based on the fact that the test bench reservoir is considerably larger than the column and has a significantly higher liquid level. Therefore,

$$h(t) = \frac{4\dot{V}t}{\pi D_{\mathrm{C}}^2} \tag{2}$$

can describe the inlet dynamics, which represent the change in height and hydrostatic pressure as a function of time t [20]. The Bernoulli equation

$$\frac{v_1^2\rho}{2} + \rho g h_1 + p_1 + \frac{\zeta v_1^2 \rho}{2} = \frac{v_2^2\rho}{2} + \rho g h_2 + p_2 \tag{3}$$

is essential for analysing the outlet dynamics, as it considers for variations in liquid height. Equation (3) accounts for frictional flow caused by the components within the outlet section, with ζ representing the total resistance coefficient and v_i denotes the velocity in the column or the outlet hose [20]. The indices refer to the positions relevant for the Bernoulli equation, namely the outlet hose (①) and the liquid level in the column (②), as illustrated in figure 1.

In deriving the analytical solution of equation (3), assumptions such as $p_1 = p_2 = p_0$, $v_2 \approx 0\,\mathrm{m\,s^{-1}}$, $h_1 = 0\,\mathrm{m}$, and $\rho = \mathrm{const.}$ are made, from which the modified Torricelli equation

$$v_1 = \sqrt{\frac{2gh_2}{1+\zeta}} \tag{4}$$

is obtained.

Equation (4) is used in conjunction with the mass balance

$$-D_{\mathrm{C}}^2 \frac{\mathrm{d}h_2}{\mathrm{d}t} = v_1 D_{\mathrm{H}}^2 \tag{5}$$

for the column [20]. The integration from h_S to $h(t)$ and 0 to t yields in

$$h(t) = \left(\sqrt{h_S} - t \left(\frac{D_H}{D_C} \right)^2 \sqrt{\frac{g}{2(1+\zeta)}} \right)^2 \tag{6}$$

as a means of characterising the dynamics of the outlet. h_S is the set starting height in the column above the outlet hose. Based on the known run-out time and rearranged equation (6) the total resistance coefficient ζ is determined at $\zeta = 19.9 \pm 0.7$. The calculated resistance coefficients are compared and verified with the values found in the literature and those provided by the manufacturer [20, 22, 23]. Moreover, a mass flow meter is employed to measure the mass flow rate at the outlet, enabling experimental validation of the outlet curve. The conversion of the mass flow rate into height as a function of time is accomplished via numerical integration of the measured values over time, incorporating the water's density and the column's cross-sectional area.

2.3. MMR

Figure 2(b) shows the MMR developed for pressure measurement applications. At the core of the sensor are two permanent magnets, separated by a distance, and a flexible membrane. One permanent magnet is a spherical neodymium magnet (N40) with a diameter of $D_{MMR,R} = 4\,mm$, referred to as the rotator. The rotator is connected to the membrane through a thin Dyneema thread (PE-UHMW) that is attached to the magnet with epoxy resin. The stator, a cylindrical diametral magnetised neodymium magnet (N35) with a diameter and height of $D_{MMR,S} = h_{MMR,S} = 4\,mm$, is fixed and embedded within the cylindrical acrylic housing. The housing has a height of $h_{MMR} = 33\,mm$ and features a base diameter of $D_{MMR} = 10\,mm$. The working principle of the MMR is based on the antiparallel arrangement of the stator and the rotator [16], which attract each other with a force several orders of magnitude greater than gravity and with the freedom for torsional oscillation. Following excitation by external magnetic fields, the rotator exhibits a damped oscillatory dynamic converging to its natural frequency f_{nat} with a high quality factor [18]. Analogue signal processing hardware is used to switch between transmit (Tx) and receive (Rx) windows with times t_{tx} (transmit) and t_{rx} (receive), thus controlling the oscillation in real-time and allowing f_{nat} to be read wirelessly. One possible way to implement a sensor is by changing the mass-centred distance d_m between both magnets to cause a desired change in frequency [18]. This is done by fixing the rotator to a flexible membrane and sealing the MMR housing. The dependence of the MMR resonance on frequency can be approximated by the dipole far field model for spheres [17] with

$$f_{nat}(d_m) = \frac{1}{2\pi} \sqrt{\frac{M_R M_S \mu_0}{4\pi d_m^3 I}} \propto d_m^{-\frac{3}{2}}\,. \tag{7}$$

The magnetic moments of the rotator and the stator M_R, M_S, vacuum permeability μ_0, mass-centred distance d_m, and the inertia I determine the resonance frequency. In this case and within the measurement range, these physical parameters are assumed to be constant and the significant parameter is the distance d_m only. The initial frequency of a sensor is $f_0 = f_{nat}(d_0)$, where d_0 refers to the equilibrium distance at atmospheric pressure p_0 and ambient temperature T_0 (sealing conditions). The mechanical range of the sensor is limited to a displacement of approximately $\Delta d \leqslant 6\,mm$, where the magnets will come into contact in the extreme case if the edge-to-edge distance between the magnets d_e approaches zero (maximum pressure). It can be observed that an initial distance exceeding $d_0 = 6\,mm$ would result in an insufficiently strong attraction and a markedly low resonance frequency when the separation of magnets becomes too large.

2.4. 3D printed elastic membrane

The MMR is equipped with a membrane fabricated using a Form 3+ 3D printer (Formlabs, USA) through the stereolithography process. The membrane material is Elastic 50A V1 (Formlabs, USA), a flexible elastomer. The membrane is approved by the manufacturer for water resistance and has a size expansion of less than 1% [24]. The membrane thickness can be precisely controlled to an accuracy of 100 μm, limited by the 3D printer. The performance and sensitivity of MMRs are significantly influenced by the thickness of the printed membrane s. The relationship between membrane thickness and pressure sensitivity is experimentally validated through a force test using a MiniZwick testing machine equipped with a 10 N load cell (ZwickRoell GmbH & Co. KG, Germany) and a 1 mm diameter punch. The test involved pressing the membrane in the centre up to a force of $F = 2\,N$, which corresponds to the expected hydrostatic pressure on the test bench. The resulting stretch distance Δd is measured in the transverse direction. Figure 3 illustrates the results for various membrane thicknesses in a range from $s = 0.5\,mm$ to $1.5\,mm$, confirming the existence of a direct correlation between thickness and sensitivity. Based on these findings, the membrane thickness must be selected based on the anticipated pressure range for the application. For this work, a membrane with a thickness of $s = 0.8\,mm$ is chosen. This thickness provides high sensitivity to small pressure variations. In contrast, the use of a thicker membrane would enable the sensor to operate across a broader pressure range, but with a reduction in sensitivity. The membrane thickness can thus be tailored to suit the specific application, representing a trade-off between sensitivity, membrane durability, and the maximum applicable pressure to the sensor, before the magnets touch.

2.5. Inductive measurement setup

To excite the passive MMR sensor, a separable square-shaped Helmholtz-like coil is used that can be joined around the base of the column (see figure 2(a)), chosen for its near homogeneous field distribution [25]. The coils differ in shape and are twice the distance from a true Helmholtz coil setup ($L = 910\,\mu H$, $R = 5.1\,\Omega$). Magnetic fields in the range of $5 - 100\,\mu T\ \mu_0^{-1}$ and 100–300 Hz are used to pump the

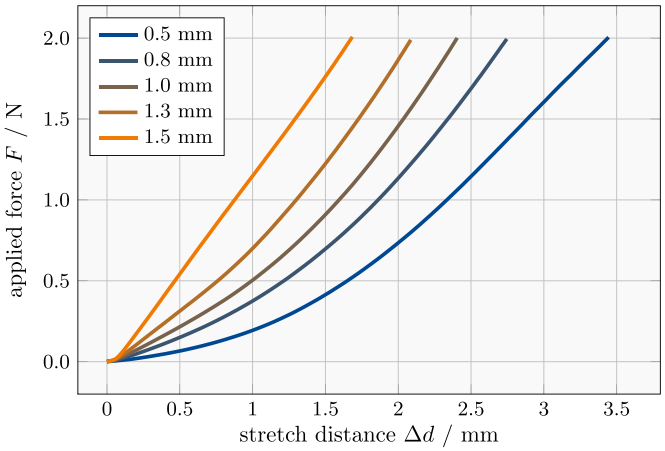

Figure 3. Membrane design and parameter choice. The stretch distance Δd in response to applied force of different membrane thicknesses between $s = 0.5$ mm and 1.5 mm thickness, 3D printed with Formlabs Elastic 50A V1 resin, are investigated with a MiniZwick testing machine with 1 mm punch.

torsional oscillation to a deflection angle of about $(11 \pm 2)\,^\circ$ during the transmit window. Based on reciprocity, the receive window is used to capture the MMR signal via the same coil pair. Transmitted signals are amplified by a class-D amplifier and received signals by a low-noise amplifier [26], both controlled by the combined RedPitaya Stemlab 125-14 DAC/ADC card operated on a custom software stack [27]. Low-level signal processing is done in real-time using frequency and phase-controlled reexcitation of the MMR. An analogue filter is used to attenuate 50 Hz harmonics in the power supply for a cleaner receive spectrum.

2.6. Sensing parameter estimation

The natural frequency f_{nat} can be determined by fitting the damped oscillator model to the measured data [16]. As neither the change over distance in equation (7) nor the stretch distance Δd of the membrane in figure 3 are linear with frequency, a calibration-based estimator is employed. The combined system is measured in a range of known static pressure levels with 20 averages (see static experiments in section 3.1). These values are fitted by a quadratic polynomial using the least squares method, and its inverse serves as an estimator of the pressure for dynamic measurements (see section 3.2). The estimator is limited to the relevant dynamic range between 0 and 100 mbar in this work and allows to derive the MMR sensitivity in Hz mbar^{-1} by taking the derivative of the polynomial fit.

2.7. Experimental procedure

Three different experimental approaches are employed: static experiments, where the pressure is kept constant over time, dynamic experiments, which aim to measure the pressure variation over time; and experiments designed to explore the temperature dependence of the MMR. Three equal MMRs (MMR A, B, C) are used for the experiments, all based on the design shown in figure 2(b). The only differences between them are the initial distances of the magnets d_0, resulting in varying initial frequencies f_0. For all experiments, MMRs are sealed at ambient temperature $T_0 = (21.1 \pm 0.5)\,^\circ$C, ensuring that the membrane is in an equilibrium state at p_0 and T_0. Furthermore, all MMRs are inserted in water before experiments to account for temperature equilibrium throughout the sensor and for minuscule membrane water uptake (see section 2.4).

The **static experiments** use a stepwise increase in pressure, where measurements are taken at constant pressure levels with at least 10 frame averages at each level. These experiments are also captured on camera to optically evaluate the changing edge-to-edge distance and are repeated for the MMR A and B. Image-based analysis are carried out in *MATLAB* (MathWorks Inc. USA), with calibration based on the known diameter of the rotator. A TxRx sequence with a long readout time is used to ensure that the exponential decay of the signal is captured to reduce errors (sequence cycle: $t_{\mathrm{tx}} = 50 \ldots 100$ ms, $t_{\mathrm{rx}} = 2000 \ldots 4000$ ms). The sensitivity in Hz mbar^{-1} is obtained by using linear regression in the lower sensor region between 0 and 100 mbar.

To capture **dynamic changes**, the liquid level is raised from 0 to ≈ 1 m in 33 s, held for 23 s, and then discharged to 0 m over 63 s. The timing is measured manually using a stopwatch (with an uncertainty of ± 1 s), and the height of the column is adjusted manually using ball valves. During this experiment, a 2 Hz frame rate is used (sequence cycle: $t_{\mathrm{tx}} = 100$ ms, $t_{\mathrm{rx}} = 400$ ms) to measure MMR A in real-time. A mass flow meter is used as an additional reference during the discharge.

In contrast to previous experiments, where the temperature is kept constant, the third experiment specifically investigates the **temperature dependence** of the MMRs. MMR C is submerged in a water tank at a constant depth, ensuring a constant hydrostatic pressure of 15 mbar. The hydrostatic pressure is influenced by the temperature due to the temperature-dependent density of water. However, within the examined temperature range, the density change is less than 2% and can therefore be regarded negligible [21]. Temperature adjustments are made with an immersion heater, and observations are based on a multimeter thermistor probe (Voltcraft VC870, Conrad Electronic SE, Germany). Upon increasing the temperature in the tank, it can be assumed that the temperature in the MMR will change rapidly compared to the surrounding water, due to the specific heat capacity of the air being four times lower than that of water [21]. The set temperatures are kept constant throughout the individual measurement process, following a protocol that used 20 averaged frames per data point (sequence cycle: $t_{\mathrm{tx}} = 200$ ms, $t_{\mathrm{rx}} = 3000$ ms).

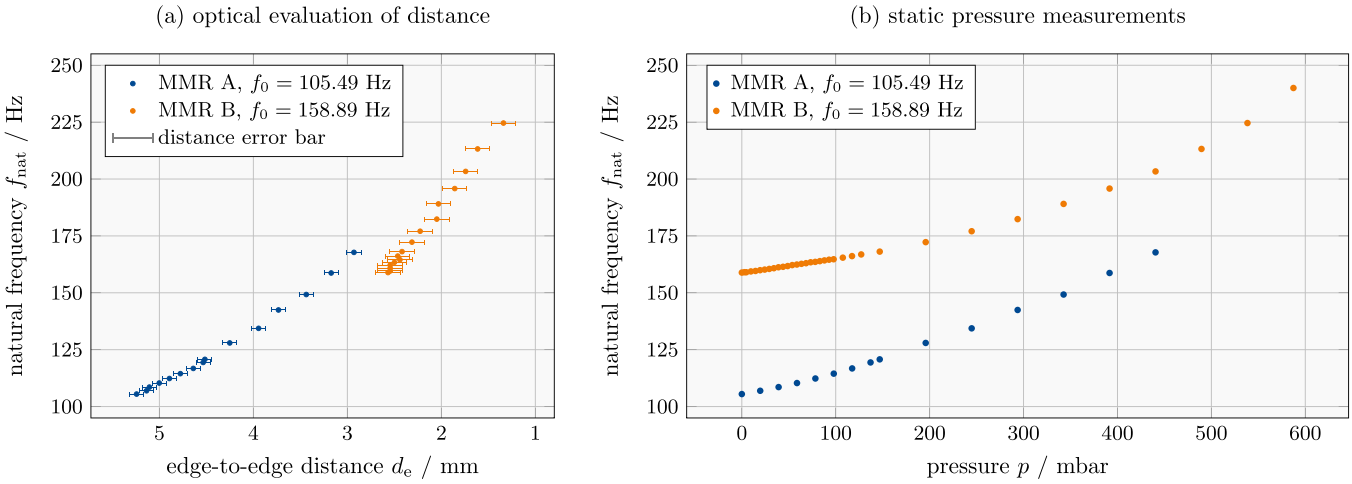

Figure 4. Results of static MMR measurements. The change in edge-to-edge distance d_e of the two magnets within the MMR is determined optically by inspecting images in (a). As the pressure increases, the membrane becomes convex and decreases the distance of stator and rotator magnets, which increases the natural frequency. The same measurements are plotted in (b), where measurements are mapped to the corresponding hydrostatic pressure of the column (optical observation). For MMR B, 10 averages per point and 5 mbar increments are used at the beginning, while for MMR A, 20 averages and 20 mbar increments are applied. For both MMRs, increments of 50 mbar are used above 150 mbar. Overall standard deviation for MMR A and B frequencies average to 0.2 Hz and 0.4 Hz, respectively.

3. Results

3.1. Static measurements

The increased pressure on the MMR sensor impresses the membrane, reducing the distance between the magnets and thus increasing the measured oscillation frequency. Optical evaluation of the edge-to-edge distance between the magnets d_e (see figure 2(b)) and the static pressure levels are shown in figures 4(a) and (b), respectively. These results illustrate the relationship between magnet separation, natural frequency, and pressure. The distance error is larger for MMR B, due to a different camera position and image resolution. The amount of plotted measurements of MMR B in figure 4(a) is reduced to improve visibility below 168 Hz. A non-linear trend of the natural frequency is observed, intensifying at small distances, which is in agreement with the results in [17] and [18]. The sensitivity of the 0.8 mm membrane sensors can be approximated with 0.07 Hz mbar^{-1} and 0.06 Hz mbar^{-1} for MMR A and B, respectively, in the region below 100 mbar. Here, the standard deviation ($n = 20$ each) in frequency of MMR A is 0.015 Hz (0.25 mbar). Throughout the total measurement range, the standard deviation for MMR A and B average to 0.2 Hz and 0.4 Hz, respectively. Sensitivity increases with decreasing distance at higher pressure, as a result of the non-linearly increasing slope of the frequency.

3.2. Dynamic measurements

The temporal performance of MMR A is tested with dynamic experiments at a frame rate of 2 Hz, which is selected for its higher sensitivity. In order to map frequency to pressure, the inverse of a least squares estimator based on previous static experiments is employed. In figure 5, the measurement of MMR A (blue) is compared with the hydrostatic pressure in the column, calculated using equations (1), (2) and (6) (orange) with the measured times for the inlet and outlet. The constant liquid levels are obtained optically, with the final level in the column determined to be $h = (99 \pm 1)$ cm, corresponding to a hydrostatic pressure of $p(h) = (96.9 \pm 0.98)$ mbar. Furthermore, the outlet is measured using the mass flow meter (green), evaluated, and included in the plot. Figure 5 confirms that equation (6) is consistent with the measurement obtained using the mass flow meter. The overall pressure measurement is also in agreement with the theory and measured pressure, with the highest deviation on the plateaus. The maximum errors of 3.7 mbar and 4.4 mbar occurred on the high and low plateaus, respectively, with an overall standard deviation of 1.57 mbar. The average zero-pressure levels at the beginning and end align within manual operation tolerances, and the membrane material does not exhibit significant hysteresis, returning to its equilibrium state at p_0 during this experiment. At stationary levels, a noisy frequency component equalling the sequence repetition frequency of 2 Hz can be observed.

3.3. Temperature dependence

Figure 6 illustrates the temperature dependence, affirming the trend that the natural frequency decreases with increasing temperature T. The effect of temperature is expected to counteract the influence of pressure on the natural frequency. This behaviour can be approximated by the ideal gas law

$$pV = mR_S T, \tag{8}$$

where R_S denotes the specific gas constant, and m, p, and V represent mass, pressure, and volume of the gas enclosed within the MMR [28]. Assuming a constant hydrostatic pressure (a valid assumption given the small temperature changes considered as explained in section 2.7), pressure and volume cannot change independently within this enclosure with the

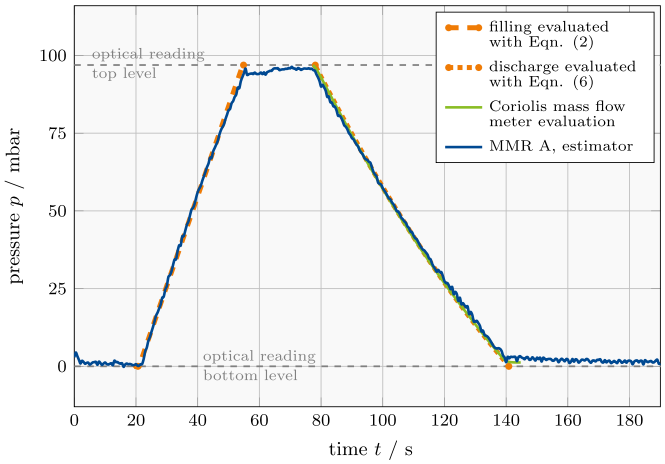

Figure 5. Dynamic MMR measurement results. Water is filled and discharged from the column, with MMR measurements taken at a 2 Hz frame rate. The natural frequency is evaluated for each time point (no averaging) and converted to pressure using an estimator based on a model fit of the static measurement. The theoretical and measured hydrostatic pressures are presented for reference, with the latter being determined through the use of a mass flow meter.

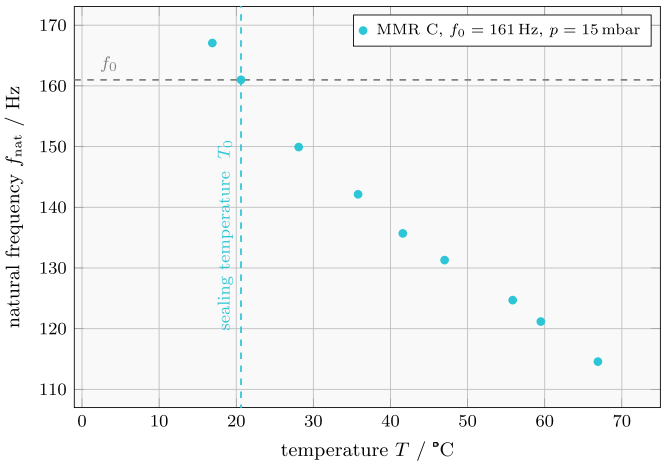

Figure 6. Temperature measurement results. The MMR is sealed at ambient temperature T_0 and an increase in the ambient water temperature (at constant pressure $p = 15$ mbar) causes a separation of the magnets, which results in a reduction in frequency.

flexible membrane. Rather, the volume rises and falls monotonically with pressure. As the temperature of the MMR increases, so does the right-hand side of the ideal gas law. In response, the factor pressure times volume will increase until they reach a new equilibrium at which point both sides of the ideal gas equation are balanced. Optical observations confirmed this behaviour, showing the membrane curving away from the casing. The severity of this effect is mainly influenced by the membrane's mechanical properties. As the membrane approaches its mechanical limits, the system transitions towards isochoric conditions, thereby diminishing the anticipated sensitivity.

As the above explanations show, the temperature effect on the distance does not follow a linear behaviour. However, within the range shown in figure 6, where the membrane operates below its mechanical limit and the hydrostatic pressure remains low, a first order linear approximation provides sufficient agreement. A linear regression of the temperature-frequency dependence is performed to provide an indication of the sensor's sensitivity to temperature changes. The resulting temperature sensitivity is $-0.98\,\mathrm{Hz\,K^{-1}}$, with a coefficient of determination r^2 of 0.985 for the measured interval.

4. Discussion

The choice of a 0.8 mm membrane thickness is shown to be durable. The most critical point in terms of mechanical stability is the membrane itself, particularly where the rotator is attached, as this area experiences the highest stress and deformation. Consequently, the overall sensor stability is largely determined by this junction. As resonant pressure sensors inherently offer better long-term stability than non-resonant types, improving this connection could enhance the overall long-term stability of the sensor [29].

Averaging of static measurements shows that the MMR pressure sensor can achieve a standard deviation of 0.25 mbar in the range 0 – 100 mbar. The standard deviation is higher for dynamic measurements at 2 Hz without averaging at 1.57 mbar, but remains below 2%. The non-linear behaviour of the sensor in figure 4 is expected from the non-linear characteristic of Δd (see figure 3) and from the dipole model assumption in equation (7) [16, 17]. However, the results show that it can be successfully calibrated based on static measurements. Higher averaging or a sufficiently accurate physical model may improve precision and accuracy.

Experiments are carried out using multiple MMRs, demonstrating that the pressure-frequency relationship is reproducible. Despite the fact that the initial gap between the manually assembled rotator and stator varies from sensor to sensor and influences the sensor characteristics, it does not affect the reproducibility of the results.

As shown in figure 6, the MMR has a significant cross-sensitivity to temperature. Although temperature sensitivity is not a design parameter in this study, as the primary focus is on assessing pressure sensitivity, future optimisations will aim to reduce the volume of air within the MMR to mitigate its influence on temperature dependence. Furthermore, it is important to acknowledge that the relationship between frequency and temperature is not linear. Therefore, it is not possible to simultaneously quantify the temperature and pressure with this MMR design. However, if one of the two parameters is known, calibration can be used to compensate for the frequency shift due to the other parameter. Moreover, modern bioprocesses, as a potential future application of MMRs, aim to maintain constant temperatures and uniform temperature distribution within bioreactor vessels [30, 31].

The absolute range of the proposed MMR sensor is restricted by the maximum stretch distance Δd, which can be modified by selecting the durability and thickness of the membrane, considering the sensitivity. With thicker membranes, the sensitivity is lower, but the pressure range is wider. A reduction in the initial distance of the sensor enhances the

Table 1. Overview of representative mechanical resonant pressure sensors in terms of sensitivity and maximum pressure.

Sensor type	Max. pressure (mbar)	Sensitivity (Hz mbar^{-1})	Reference
Industrial MMR	600	0.06	Present study
Medical MMR	400	0.34	[16]
MoS_2 membrane sensor	500	578 000	[32]
Graphene squeeze-film sensor	1000	9000	[33]
Dual-diaphragm coupled sensor	1900	0.8	[34]
Piezoresistively detected sensor	2000	1.9	[35]

sensitivity due to the increased slope, which in turn restricts the range. The thickness of the membrane and the initial magnet distance should therefore be tailored to the specific requirements of the application.

The accuracy of calculating f_{nat} depends on the input parameters of the model such as windowing and iterations, and on the convergence of the model [17]. The deviation between the modelled pressure and estimator MMR pressure in figure 5, depends on the fit and the static pressure levels in figure 4. The results can be further improved by using closer spaced calibration values and more averages.

The presence of electromagnetic noise and distorted supply currents in process engineering do not affect the sensitivity at the specified distance. The detection limitations of passive resonant sensors are based on the steep drop in signal-to-noise ratio (SNR) due to distance, which is further deteriorated by conductive fluids or vessels due to eddy currents. The experiments presented in this study are conducted within a transparent and non-conductive column. However, industrial vessels are generally manufactured from optically inaccessible and conductive materials (in process engineering). In this case, a promising result is observed in an experiment in which the inductive measurement setup is tested with a non-transparent, conductive column made from 1 mm thick aluminium, which results in a reduction of the SNR by approximately a factor of two.

On the other hand, the emitted sensor signal has an upper limit determined by physical parameters such as frequency (induction), deflection angle, and magnetic moment (sensor size), even if excitation is achieved at larger distances using high and pulsed currents. Increasing the SNR can be achieved with ultra-low noise amplifiers, dedicated receiving coils, and stronger magnetic materials (N52 or higher). The 2 Hz sensor readout frequency reflects the current sensor's limitation, but higher frame rates allowing faster data acquisition and more averaging could be achieved using smaller, faster-oscillating MMRs and shorter receive windows, at the cost of increased sensing uncertainty. Furthermore, sensor latency, defined as the time between a measurable stimulus and the corresponding digital output, is mainly influenced by the receive window length and processing delay. It can be reduced, for example by using more efficient methods to estimate the natural frequency, though this may increase sensing uncertainty.

As mentioned in section 1, MMRs are intended for future use as Lagrangian sensor particles in industrial applications. While current Lagrangian sensor particles employ commercial piezoresistive pressure sensors with a maximum range of 6000 mbar and a resolution of 9 Pa [15], the (industrial) MMR developed in this study does not match the performance of these commercial pressure sensors. In addition, mechanical resonant pressure sensors have been the subject of substantial research efforts, as reviewed in [29]. Table 1 provides an overview of the representative sensor concepts in terms of sensitivity and maximum pressure. Compared to other mechanical resonant pressure sensors, the industrial MMRs exhibit lower sensitivity and operate at a lower maximum pressure range. Nevertheless, the industrial MMRs still offer potential for the use in process engineering. Their main advantages are three-dimensional trackability and fully wireless, passive operation, enabling applications in bioreactors where other sensors are limited. Moreover, trackable MMRs have already been investigated in the context of medical applications. For example, Gleich *et al* [16] presented a miniaturised MMR with a compressible housing for pressure sensing. In comparison, the industrial MMR is designed to operate over a broader pressure range. While the medical MMR demonstrates higher sensitivity, the sensor presented here is tailored for wider applicability in process engineering. However, there is considerable scope for improvement and optimisation in all aspects of the presented sensor, including its manufacturing process, the mechanism by which pressure is coupled to frequency (housing design) via a single membrane, and signal detection equipment.

The technology is well suited to environments typically encountered in industrial process engineering. The specific operating conditions of an MMR sensor are largely determined by the material properties of its components. The sensor presented in this study is designed to withstand conditions common in bioprocesses, including standard operating temperatures, hydrostatic pressures up to 600 mbar (corresponding reactor height of approximately 6 m), and exposure to non-corrosive or mildly aggressive media. Due to the ability to tailor housing materials, the MMR sensor can be adapted to withstand more demanding environments involving elevated temperatures, increased pressures, or chemically aggressive media. Additionally, the measurement technology can operate through acrylic glass and water. However, further investigations are required to assess the penetration capabilities of reactor materials and media. Moreover, the design of the MMR housing is fundamental to address the central challenges

laid out in this work. These include sensitivity to pressure, cross-sensitivity to temperature, and buoyancy. This proof of concept demonstrates that MMRs can be utilised for sensing in industrial environments. Consequently, future developments should focus on advancing the MMR technology for the use as Lagrangian sensor particles. Thus, MMRs will be further developed to enable flow-following capabilities. To achieve this, the density of the MMR must be adjusted to match that of the surrounding medium. Since the MMRs tested in this study exhibit positive buoyancy in water, the volume of air within the MMRs needs to be reduced or replaced with alternative media, such as gel.

5. Conclusion

An MMR pressure sensor has been successfully developed and tested. The sensor employs a 0.8 mm 3D printed flexible membrane. The adaptability of the additive manufacturing process allows for the modification of membrane geometry and material to align with the desired pressure sensitivity, pressure range, and specific application. The MMR design demonstrates a minimum sensitivity of 0.06 Hz $mbar^{-1}$, with sensitivity increasing at higher pressures, which makes it suitable for process engineering applications. The relationship between frequency and pressure is non-linear and requires calibration, for example, using a model fit of static measurements. Additionally, the sensor's maximum pressure of 600 mbar, approximately equivalent to a hydrostatic pressure of 6 m, accommodates a wide range of reactors commonly used in the field. Analysis of dynamic measurements reveals an average accuracy of 1.57 mbar. Averaging the real-time readout at 2 Hz can enhance the accuracy of the measurement, depending on the desired dynamic constraints. The MMR exhibits notable cross-sensitivity to temperature with $-0.98\,Hz\,K^{-1}$.

A significant advantage of MMR pressure sensors over Lagrangian sensor particles is their ability to be localised in terms of position and orientation within the reactor [16], wirelessly and through opaque fluids such as emulsions, flows with high cell or bubble densities, and optically inaccessible materials. Additionally, the MMRs are passive, negating the need for a power supply and thereby simplifying the device's design, which also enables cost-effective manufacturing. This measurement principle further eliminates the risk of battery-derived hazardous substances, enhancing their suitability for industrial bioreactors.

Data availability statement

The data that support the findings of this study are openly available at the following URL/DOI: https://doi.org/10.15 480/882.14 543 [36].

Acknowledgments

T M printed the 3D membranes and supervised the force experiments. T M, J F, and F M manufactured the MMR sensors. T M, F K, J F, and F M conducted experiments 3.1 and 3.2. F M and J F conducted experiment 3.3. M S, T K, T M, M M, F K, J F, and F M contributed to the conceptualisation and theory. M S and T K supervised the project. T M and F M wrote the original draft with support from F K, J F, and M M. All authors reviewed the final manuscript. The authors would like to thank Furkan Kahraman for his help in building the separable Helmholtz coil. Publishing fees supported by Funding Program Open Access Publishing of Hamburg University of Technology (TUHH). This project is funded by the Deutsche Forschungsgemeinschaft (DFG, German Research Foundation) – SFB 1615 – 503850735.

ORCID iDs

Timo Merbach 0000-0002-7723-5444
Felix Kexel 0000-0003-4268-2348
Jonas Faltinath 0009-0003-4128-2948
Martin Möddel 0000-0002-4737-7863
Michael Schlüter 0000-0001-5969-2150
Tobias Knopp 0000-0002-1589-8517
Fabian Mohn 0000-0002-9151-9929

References

[1] Siebler F, Lapin A, Hermann M and Takors R 2019 The impact of CO gradients on C. ljungdahlii in a 125 m^3 bubble column: mass transfer, circulation time and lifeline analysis *Chem. Eng. Sci.* **207** 410–23
[2] Vrábel P, van der Lans R G, Luyben K C A, Boon L and Nienow A W 2000 Mixing in large-scale vessels stirred with multiple radial or radial and axial up-pumping impellers: modelling and measurements *Chem. Eng. Sci.* **55** 5881–96
[3] Rosseburg A, Fitschen J, Wutz J, Wucherpfennig T and Schlüter M 2018 Hydrodynamic inhomogeneities in large scale stirred tanks–influence on mixing time *Chem. Eng. Sci.* **188** 208–20
[4] Buntkiel L, Ma Y, Reinecke S F and Hampel U 2023 Orientation resolved measurements of accelerations with sensor particles in bioreactors *tm-Technisches Messen* **90** 835–45
[5] Hofmann S *et al* 2024 Experimental analysis of lifelines in a 15,000 L bioreactor by means of Lagrangian sensor particles *Chem. Eng. Res. Des.* **205** 695–712
[6] Bisgaard J, Muldbak M, Tajsoleiman T, Rydal T, Rasmussen T, Huusom J K and Gernaey K V 2021 Characterization of mixing performance in bioreactors using flow-following sensor devices *Chem. Eng. Res. Des.* **174** 471–85
[7] Rautenbach R, Hofmann S, Buntkiel L, Schäfer J, Reinecke S F, Hoffmann M, Hampel U and Schlüter M 2024 Dynamics of Lagrangian sensor particles: the effect of non-homogeneous mass distribution *Processes* **12** 1617
[8] Stine J M, Beardslee L A, Sathyam R M, Bentley W E and Ghodssi R 2020 Electrochemical dissolved oxygen sensor-integrated platform for wireless *in situ* bioprocess monitoring *Sens. Actuators B* **320** 128381
[9] Lauterbach T *et al* 2019 Measurements on the fly–introducing mobile micro-sensors for biotechnological applications *Sens. Actuators A* **287** 29–38
[10] Kuschel M, Siebler F and Takors R 2017 Lagrangian trajectories to predict the formation of population heterogeneity in large-scale bioreactors *Bioengineering* **4** 27

[11] Haringa C, Noorman H J and Mudde R F 2017 Lagrangian modeling of hydrodynamic–kinetic interactions in (bio) chemical reactors: practical implementation and setup guidelines *Chem. Eng. Sci.* **157** 159–68
[12] Lara A R, Galindo E, Ramírez O T and Palomares L A 2006 Living with heterogeneities in bioreactors: understanding the effects of environmental gradients on cells *Mol. Biotechnol.* **34** 355–81
[13] Wang G, Tang W, Xia J, Chu J, Noorman H and van Gulik W M 2015 Integration of microbial kinetics and fluid dynamics toward model-driven scale-up of industrial bioprocesses *Eng. Life Sci.* **15** 20–29
[14] Heins A-L and Weuster-Botz D 2018 Population heterogeneity in microbial bioprocesses: origin, analysis, mechanisms and future perspectives *Bioprocess Biosyst. Eng.* **41** 889–916
[15] Hofmann S *et al* 2025 Lagrangian sensor particles for detecting hydrodynamic heterogeneities in industrial bioreactors: experimental analysis and lattice-boltzmann simulations *Chem. Eng. J. Adv.* **22** 100744
[16] Gleich B, Schmale I, Nielsen T and Rahmer J 2023 Miniature magneto-mechanical resonators for wireless tracking and sensing *Science* **380** 966–71
[17] Knopp T, Mohn F, Foerger F, Thieben F, Hackelberg N, Faltinath J, Tsanda A, Boberg M and Möddel M 2024 Empirical study of magnet distance on magneto-mechanical resonance frequency *Curr. Dir. Biomed. Eng.* **10** 377–80
[18] Faltinath J, Mohn F, Foerger F, Möddel M and Knopp T 2025 Natural frequency dependency of magneto-mechanical resonators on magnet distance (arXiv:2503.04520)
[19] Pascal B 1663 Traitez de l'Equilibre des Liqueurs (Treatise on the Equilibrium of Fluids)
[20] Spurk J and Aksel N 2020 *Fluid Mechanics* (Springer)
[21] Stephan P, Kabelac S, Kind M, Mewes D, Schaber K and Wetzel T 2019 *VDI-Wärmeatlas: Fachlicher Träger VDI-Gesellschaft Verfahrenstechnik und Chemieingenieurwesen* (Springer)
[22] Idelchik I E 1994 *Handbook of Hydraulic Resistance* 3rd edn (Begell House)
[23] Endress & Hauser 2024 Proline promass 80 (available at: https://bdih-download.endress.com/files/DLA/50721CA194500164E10000000A35E042/BA00057DDE_1312.pdf/) (Accessed 12 December 2024)
[24] Formlabs 2020 Elastic 50a, resin for soft flexible parts (available at: https://formlabs-media.formlabs.com/datasheets/2001420-TDS-ENUS-0.pdf) (Accessed 8 November 2024)
[25] Hurtado-Velasco R and Gonzalez-Llorente J 2016 Simulation of the magnetic field generated by square shape Helmholtz coils *Appl. Math. Modelling* **40** 9835–47
[26] Mohn F, Thieben F and Knopp T 2025 Low-cost analog signal chain for transmit-receive circuits of passive induction-based resonators (arXiv:2502.03202)
[27] Hackelberg N, Schumacher J, Graeser M and Knopp T 2022 A flexible high-performance signal generation and digitization plattform based on low-cost hardware *Int. J. Magn. Part. Imaging* **8** 2203063
[28] Schmidt A 2019 *Technical Thermodynamics for Engineers* (Springer)
[29] Dinh T, Rais-Zadeh M, Nguyen T, Phan H-P, Song P, Deo R, Dao D, Nguyen N-T and Bell J 2024 Micromachined mechanical resonant sensors: from materials, structural designs to applications *Adv. Mater. Technol.* **9** 2300913
[30] Simutis R and Lübbert A 2015 Bioreactor control improves bioprocess performance *Biotech. J.* **10** 1115–30
[31] Kumar M, Prasad D, Giri B S and Singh R S 2019 Temperature control of fermentation bioreactor for ethanol production using IMC-PID controller *Biotechnol. Rep.* **22** e00319
[32] Lee J and Feng P X-L 2014 Atomically-thin MoS_2 resonators for pressure sensing *2014 IEEE Int. Frequency Control Symp. (FCS)* (IEEE) pp 1–4
[33] Dolleman R J, Davidovikj D, Cartamil-Bueno S J, van der Zant H S and Steeneken P G 2016 Graphene squeeze-film pressure sensors *Nano Lett.* **16** 568–71
[34] Du X, Liu Y, Li A, Zhou Z, Sun D and Wang L 2016 Laterally driven resonant pressure sensor with etched silicon dual diaphragms and combined beams *Sensors* **16** 158
[35] Han X *et al* 2020 Novel resonant pressure sensor based on piezoresistive detection and symmetrical in-plane mode vibration *Microsyst. Nanoeng.* **6** 95
[36] Merbach T, Kexel F, Faltinath J, Möddel M, Schlüter M, Knopp T and Mohn F 2025 Data supplement for publication: wireless and passive pressure detection using magneto-mechanical resonances in process engineering *TUHH Open Research (TORE)* 10.15480/882.14543